ACSNANO

www.acsnano.org

ARTICLE

MX Anti-MXenes from Non-van der Waals Bulks for Electrochemical Applications: The Merit of Metallicity and Active Basal Plane

Jinxing Gu, Ziyuan Zhao, Jingsong Huang,* Bobby G. Sumpter, and Zhongfang Chen*

Cite This: *ACS Nano* 2021, 15, 6233–6242

Read Online

ACCESS | Metrics & More | Article Recommendations | Supporting Information

ABSTRACT: Two-dimensional transition-metal compounds (2DTMCs) are promising materials for electrochemical applications, but 2DTMCs with metallicity and active basal planes are rare. In this work, we proposed a simple and effective strategy to extract 2DTMCs from non-van der Waals bulk materials and established a material library of 79 2DTMCs, which we named as anti-MXenes since they are composed of one M atomic layer sandwiched by two X atomic layers. By means of density functional theory computations, 24 anti-MXenes were confirmed to be thermodynamically, dynamically, mechanically, and thermally stable. The metallicity and active basal plane endow these anti-MXenes with potential as excellent electrode materials, for example, as electrocatalysts for hydrogen evolution reactions (HER). Among the noble-metal free anti-MXenes with favorable H-binding, CuS can boost HER at the whole range of H coverages, while CoSi, FeB, CoB, and CoP show promise for HER at some specific H coverages. The active sites are the tetra-coordinating nonmetal atoms at the basal planes, thus rendering a very high density of active sites for these materials. CoB is also a promising anode material for lithium-ion batteries, showing low Li diffusion energy barriers, a very high capacity, and a suitable open circuit voltage. This work promotes the "computational exfoliation" of 2D materials from non-van der Waals bulks and exemplifies the applications of anti-MXenes in various electrochemical processes.

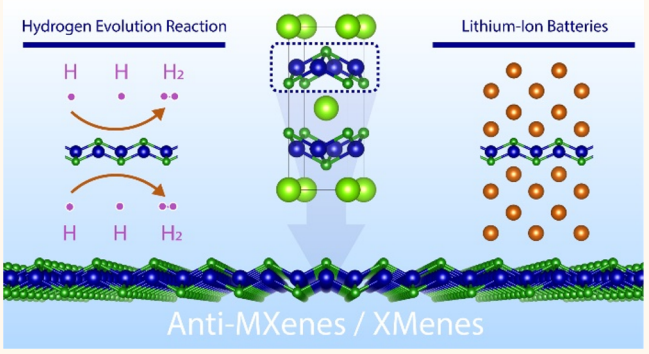

KEYWORDS: *anti-MXenes, non-van der Waals bulks, metallicity, active basal plane, hydrogen evolution reaction, lithium-ion batteries*

Hydrogen (H_2) is a potential energy resource for substituting conventional fossil fuels.[1] Currently, hydrogen is mostly produced from fossil fuels by steam methane reforming and partial oxidation and coal gasification. Unfortunately, these industrial methods not only consume fossil fuels but also release greenhouse gases.[2] Water electrolysis, instead, provides an ecofriendly and sustainable way to generate H_2 *via* hydrogen evolution reaction (HER).[3] Note that HER usually exhibits a high overpotential, which significantly hinders the effectiveness of water splitting,[4] and therefore electrocatalysts must be used to facilitate HER.[5,6] Up to now, platinum nanoparticles supported on carbon are widely used in industry due to the extremely high exchange current density and small Tafel slope.[7] However, the scarcity, high cost, and low stability restrict large-scale applications of Pt-based catalysts. Under this backdrop, developing noble-metal-free electrocatalysts is of tremendous interest.[6]

Among various noble-metal-free materials, two-dimensional transition-metal compounds (2DTMCs) have highly distinguished themselves:[8−14] They not only inherit advantages from conventional 2D materials,[15] such as the large specific surface areas, tunable electronic properties, and robust mechanic structures,[16−18] but also have diverse chemical compositions that are earth abundant. To date, various 2DTMCs have been investigated as electrocatalysts for HER, including transition-metal chalcogenides,[19−22] phosphides,[23−25] carbides,[11,26−28] and borides.[29,30] A typical 2DTMC with good HER activity is the 1H phase of MoS_2,[31,32] which shows an exchange current density in the magnitude of 10^{-7} A/cm^2 and a Gibbs free energy of H adsorption (ΔG_{*H}) of 0.08 eV.[33,34] However, the density of active sites of 1H MoS_2 is very low, because its catalytic performance is attributed to sulfur atoms only at edge

Received: October 8, 2020
Accepted: February 23, 2021
Published: March 18, 2021

https://dx.doi.org/10.1021/acsnano.0c08429
ACS Nano 2021, 15, 6233–6242

positions rather than those at basal planes.[33] The active sulfur atoms at edges are dicoordinating, while the inert sulfur atoms at basal planes are tricoordinating.[33,35] This difference suggests an effect of atomic coordination environment, which in turn prompts a question whether sulfur atoms at the basal planes of 2DTMCs with a modified coordination number (*e.g.*, tetra-coordinating sulfur atoms) could exhibit a distinct and beneficial catalytic performance toward HER. Such an effect also exists in other reactions: For metal−nitrogen−carbon single-atom catalysts, the single Fe/Cu atoms coordinated by two N atoms exhibit the best performance for N_2/O_2 reduction than those with other coordination scenarios.[36,37] Additionally, 1H MoS_2 is a semiconductor with a band gap about 1.8 eV,[38] which means a nonideal charge transport performance at the electrode for catalysis.[39] Other 2DTMCs face similar problems toward HER, that is, the impeded conductivity and low density of active sites.[20] Therefore, it is desirable to search for 2DTMCs with metallic electronic properties and high-density active basal planes.[40−48]

FeSe-like 2DTMCs caught our attention, due to their excellent electronic and structural properties.[49−51] Their metallic conduction and tetra-coordinating nonmetal atoms at the basal plane hint at a great potential as HER electrocatalysts, and yet their activity toward HER has not been systematically considered. The chemical formula of FeSe-like 2DTMCs is expressed as MX, where M represents transition metals and X represents nonmetals. Their geometry is composed of one M atomic layer sandwiched by two X atomic layers. Compared with transition-metal dichalcogenides such as MoS_2, the increased metal/nonmetal ratio of FeSe-like 2DTMCs could benefit the charge transport performance. Unlike conventional 2D materials that are exfoliated from layered bulks, FeSe-like 2DTMCs are mainly found in KFe_2S_2-like non-van der Waals bulk materials,[52,53] in which 2D sublayers are held together by ionic interactions instead of van der Waals interactions. Encouragingly, it is experimentally feasible to fabricate FeSe-like 2DTMCs by transforming non-van der Waals bulks to van der Waals bulks.[54,55] A good exemplar is the discovery of MXenes, which are 2D sublayers inside MAX phases.[11,12,39,56] MXenes without functional groups can be denoted in the formula as $M_{n+1}X_n$, where the nonmetal atomic layers are sandwiched by metal atomic layers.[57]

Since the stacking sequence of atomic layers in FeSe-like 2DTMCs is in direct contrast to that in MXenes, we named these FeSe-like 2DTMCs as anti-MXenes, following the concept to name anti-MoS_2.[58] Alternatively, these FeSe-like 2DTMCs can be called XMenes (pronounced as "cross-meens") for simplicity to reflect their difference from MXenes in terms of the stacking sequence of atomic layers. Correspondingly, the precursor bulk materials for XMene synthesis can be termed as a XAM phase (pronounced as "cross-am" phase), similar to the precursor bulk MAX phase for MXene synthesis. To establish a material library of anti-MXenes (or simply XMenes) and explore their catalytic performance toward HER, the traditional trial and error experimental approach is too time-consuming and costly, while modern computational techniques offer a promising approach due to their strong predictive ability for the discovery and design of 2D materials.[59−61] To date, most of the computational explorations of 2D materials focused on predicting 2D materials from van der Waals bulks in a variety of databases.[62−69]

In this work, we developed a simple and effective strategy to predict anti-MXenes from non-van der Waals bulk materials and evaluated their catalytic performance for electrochemical applications. Using this strategy, a material library containing 79 anti-MXenes was established, 24 of which were confirmed to be rather stable and metallic. With regard to the HER catalytic activity, CoSi and FeB show high performance at a high H coverage, while CoB and CoP show high performance at a low H coverage. In comparison, CuS exhibits a high density of active sites and can boost HER under the whole range of H coverages. These anti-MXenes also show promise as anode materials for lithium-ion batteries (LIBs). For example, CoB exhibits small diffusion energy barriers and a high capacity for lithium ions as well as a suitable open circuit voltage. This work exemplifies the exfoliation of 2D materials from non-van der Waals bulk materials and calls for more research efforts on exploring anti-MXenes for electrocatalysis and other related fields.

RESULTS AND DISCUSSION

Extraction of Anti-MXenes from Database. Anti-MXenes are sublayers of the KFe_2Se_2-like non-van der Waals bulk materials, where the neighboring 2D sublayers are held together by ionic interactions rather than van der Waals interactions (Figure 1a). The chemical formula of KFe_2Se_2-like

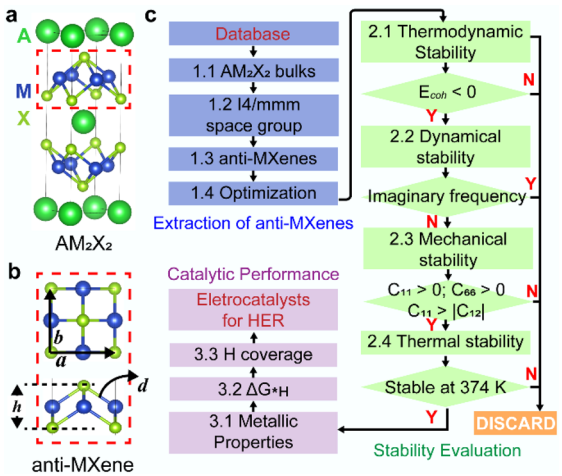

Figure 1. Anti-MXenes as well as the strategy to obtain anti-MXenes and to evaluate their catalytic performance toward HER. (a) Schematic structure of AM_2X_2 bulks with *I*4/*mmm* space group. (b) Schematic geometry of anti-MXene from the top and the side view. (c) Procedure to extract anti-MXenes and to screen HER electrocatalysts.

bulk materials can be in general expressed as AM_2X_2, where A represents alkali, alkaline earth, lanthanide, or actinide metals, while M and X are transition metals and nonmetal elements, respectively. Correspondingly, sublayer anti-MXenes are composed of two M and two X atoms inside a unit cell, which is of a square shape ($a = b$) in a bird's eye view (Figure 1b, top). The vertical distance between two X atoms from the top and bottom atomic layers is denoted as height h, while the bond lengths of M−X bonds are denoted as distance d (Figure 1b, bottom).

To obtain anti-MXenes and to screen for the best HER catalysts, we utilized the screening procedure as illustrated in Figure 1c, which goes sequentially through an extraction step

https://dx.doi.org/10.1021/acsnano.0c08429
ACS Nano 2021, 15, 6233−6242

to extract the structures from the database for optimization, a stability evaluation step to analyze stabilities, and a catalytic performance examination step to analyze HER activities. In the extraction step, 2575 AM_2X_2 bulks were retrieved from the Materials Project database,[70] where 636 AM_2X_2 bulks belong to the space group of $I4/mmm$. Because most of the 636 bulks present the same target 2D sublayer with a difference only in the A elements, the final number of extracted anti-MXenes is less than the number of bulks. Accordingly, by removing the element A, a library containing 79 anti-MXenes was established. The optimized structural parameters of these 79 anti-MXenes are listed in Table S1.

Evaluation of Stabilities. We expected that not all of the 79 anti-MXenes are of significant stability to ensure their experimental realization. Thus, in the stability evaluation step, we systematically evaluated their thermodynamic, dynamical, mechanical, and thermal stabilities (Figure 1c). The thermodynamic stabilities of anti-MXenes were evaluated by the cohesive energy (E_{coh}), defined as $E_{coh} = (E_{MX} - 2E_M - 2E_X)/4$, where E_{MX}, E_M, and E_X are total energies of the anti-MXene unit cell, the isolated transition metal, and the isolated nonmetal atom, respectively. All the 79 extracted anti-MXenes satisfy the thermodynamic stability criterion of $E_{coh} < 0$ (Table S2). The dynamic stabilities of these anti-MXenes were evaluated by the phonon dispersion calculations. Out of these 79 thermodynamically stable anti-MXenes, 31 anti-MXenes are dynamically stable as determined by not presenting imaginary phonon frequencies (Figure S1), while 10 have small imaginary frequencies (Figure S2), and 38 present large imaginary frequencies (Figure S3). Then, we examined the mechanical stabilities of these dynamically stable anti-MXenes by calculating their elastic constants.[71] Using the mechanical stability criteria: $C_{11}C_{22} - C_{12}^2 > 0$, and $C_{66} > 0$ (Table S3), we found that 26 anti-MXenes are mechanically stable. The thermal stabilities of the above obtained 26 anti-MXenes were evaluated by AIMD simulations at 374 K for 20 ps.[72] The temperature was set to 374 K, because we suggest that these anti-MXenes can be fabricated in an aqueous solution similar to MXenes,[73] where the temperature is limited by the boiling point of water. These simulations exclude two materials (CuSe and PdP), as they present dramatical structural deformations (Figure S4).

The above thorough evaluation of stabilities led to 24 anti-MXenes as stable 2D materials. Figure 2 illustrates eight representatives structures of the 24 anti-MXenes, showing that anti-MXenes well preserve the geometry from the XAM phases. Besides FeSe,[74] MnAs and MnP,[75] CoS, CoSe, and NiS[76] which were reported previously, the anti-MXenes family also includes three borides (CoB, FeB, and IrB), four silicides (CoSi, IrSi, PtSi, and TcSi), four arsenides (CoAs, CrAs, RhAs, and RuAs), five phosphides (CoP, IrP, OsP, RhP, and RuP), one sulfide (CuS), and one germanide (IrGe). These structures are not available in Materials Project database, Materialsweb database (which reported another anti-MXene, namely CuBr),[65] or 2DMatPedia (which contains CuBr, CoS, CoSe, NiS, and TiSe).[48,76] Note that CuBr and TiSe exist in their van der Waals bulks and thus were not revealed by our method. Likewise, the originally called rocksalt ZnSe single-layer sheet, which was predicted based on its parent covalent bulk structure,[77−79] was not found by our method. The rediscovery of FeSe, MnAs, MnP, CoS, CoSe, and NiS demonstrates the reliability and predictive power of our screening procedure.

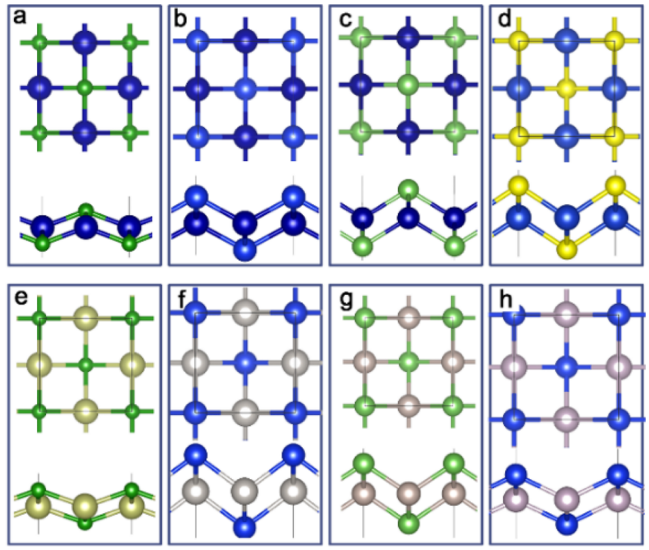

Figure 2. Optimized structures of eight representative stable anti-MXenes: (a) CoB, (b) CoSi, (c) CrAs, (d) CuS, (e) IrB, (f) PtSi, (g) RuAs, and (h) TcSi.

Due to the symmetry of anti-MXenes, the lattice constant ($a = b$) has a correlation with the M−X bond length (d) and the height (h) as $4d^2 = a^2 + h^2$ (Table 1). Generally, the lattice constants of the 24 anti-MXenes are in the range of 3.57−4.27 Å, the heights are between 1.19 and 2.95 Å, and the M−X bond lengths are from 1.91 to 2.45 Å. Among these anti-MXenes, TcSi has the largest lattice constant (4.27 Å), and PtSi has the largest height (2.95 Å) and the longest M−X bond length (2.45 Å). In comparison, CoP shows the smallest lattice

Table 1. Lattice Constants, Heights, Bond Lengths, and Cohesive Energies of 24 Stable anti-MXenes

anti-MXenes	$a = b$ (Å)	h (Å)	d (Å)	E_{coh} (eV/atom)
CoAs	3.64	2.80	2.30	−4.27
CoB	3.58	1.33	1.91	−5.36
CoP	3.57	2.53	2.19	−4.71
CoS[a]	3.63	2.41	2.18	−4.60
CoSe[a]	3.65	2.84	2.31	−4.21
CoSi	3.83	2.13	2.19	−4.63
CrAs	4.17	2.53	2.44	−3.33
CuS	3.88	2.48	2.30	−3.30
FeB	3.69	1.19	1.94	−4.96
FeSe[a]	3.68	2.77	2.30	−4.01
IrB	3.91	1.38	2.07	−6.67
IrGe	4.12	2.61	2.44	−5.30
IrP	3.91	2.61	2.35	−5.80
IrSi	4.11	2.25	2.34	−5.96
MnAs[a]	3.84	2.82	2.38	−3.41
MnP[a]	3.76	2.51	2.26	−3.85
NiS[a]	3.80	2.28	2.21	−4.20
OsP	4.03	2.31	2.32	−5.81
PtSi	3.92	2.95	2.45	−5.19
RhAs	3.94	2.86	2.44	−4.78
RhP	3.88	2.58	2.33	−5.16
RuAs	4.03	2.68	2.42	−4.81
RuP	4.04	2.16	2.29	−5.37
TcSi	4.27	2.01	2.36	−5.06

[a]Reported previously in refs 74−76.

https://dx.doi.org/10.1021/acsnano.0c08429
ACS Nano 2021, 15, 6233−6242

constant (3.57 Å), FeB features the smallest height (1.19 Å), and CoB features the shortest M−X bond length (1.91 Å).

The cohesive energies of the 24 anti-MXenes range from −3.00 to −6.67 eV/atom (Table 1). In general, the smaller the atomic number of the X atom, the more negative the cohesive energy. These cohesive energies are less negative than that of graphene (−9.91 eV/atom),[80] but are comparable to or even lower than that of the experimentally synthesized phosphorene (−3.61 eV/atom),[81] confirming the thermodynamic stabilities of these anti-MXenes. The calculated Young's moduli of the 24 anti-MXenes range from 2.80 to 102.72 N/m (Table S3), smaller than that of graphene (340.8 N/m) or MoS_2(129 N/m).[82,83] Compared to the Young's modulus of 36.82 N/m for FeSe, many anti-MXenes show enhanced mechanical strength than FeSe. The dynamic and thermal stabilities of the 24 anti-MXenes are summarized in Figures S1−S4.

For the 24 anti-MXenes, the static exfoliation energy (E_{exf}) and the relative formation energy (or energy above hull, denoted as E_{rfe}) are calculated to provide comprehensive evaluations of their potential for experimental fabrications. According to previous works,[84−86] the E_{exf} for our systems is defined as $E_{exf} = (2E_{MX} + 2E_A - E_{XAM})/4S$, where E_{MX}, E_{XAM}, and E_A are total energies of the anti-MXene, XAM bulk containing 2 A atoms and two MX units, the single atom of A in its most stable bulk, and S is the surface area of the corresponding anti-MXene. The results show that FeSe anti-MXene is the easiest for experimental exfoliation, as its static exfoliation energy is 0.003 eV/Å^2 (Table S4). In addition, CoSe, NiS, RhAs, CoS, CoAs CrAs, MnAs, IrP, and RhP have good potential to be exfoliated, since their static exfoliation energies are <0.100 eV/Å^2. It is reported that among the synthesized MXenes, V_2C shows the largest exfoliation energy of 0.205 eV/Å^2.[84] In this work, the largest value of the exfoliation energies is 0.170 eV/ Å^2 for CoSi eV/Å^2, indicating that all these 24 anti-MXenes have a high feasibility for experimental realization. The relative formation energy (E_{rfe}) reveals the stability of anti-MXene against the most stable phase. Usually, 2D materials are less stable than their three-dimensional bulks due to the large surface energy, which means that the E_{rfe} of 2D materials are positive, and a smaller value of E_{rfe} indicates higher stability. For example, the synthesized $M_{(n+1)}X_nO_2$ MXenes all present positive E_{rfe} values, and the largest E_{rfe} for the synthesized $M_{(n+1)}X_nO_2$ MXenes is +0.285 eV/atom for V_2CO_2.[87] Using this value (+0.285 eV/atom) as a reference, we found that 11 anti-MXenes are qualified for easy fabrication (Table S5). FeSe is still the easiest one for fabrication, followed by CoSe, CoS, NiS, RhAs, MnAs, CoAs, CuS, IrP, RhP, and CoP.

To help understand the high stabilities, we investigated the bonding properties of these 24 anti-MXenes by scrutinizing the charge density difference (CDD) and the electron localization function (ELF). CDD plots indicate the charge flows between the M and X atoms. The charge density difference $\Delta\rho$ for M and X becoming MX is defined as $\Delta\rho = \rho_{MX} - \rho_M - \rho_X$, where ρ_i is the charge density of i (i = MX, M, and X). A positive value of $\Delta\rho$ means the accumulation of charges, while a negative value means the depletion of charges (Figure S5). Taking CoB as an example (Figure 3a), a large portion of the charge depletion is around the d orbitals of the transition metal. In general, for these 24 anti-MXenes, depleted charges accumulate around M−X chemical bonds and are closer to the X atoms. The ELF plots (Figure 3b and Figure S6) further revealed that electrons are mainly located around the X atoms.

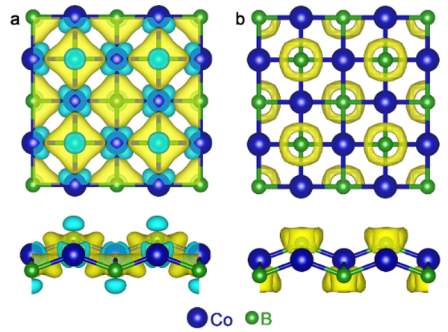

Figure 3. Bonding properties of CoB. (a) Charge density difference plot, where the isosurface value is 0.009. Yellow color denotes charge accumulation, while blue color denotes charge depletion. (b) ELF plot, where the isosurface value is 0.7. Note that the values of 1.0 and 0.5 represent the perfect localization and the free electron gas, while the value near zero denotes a low electron density area.

Thus, both CDD and ELF plots clearly show that M−X bonds in these anti-MXenes are of significant ionic character, which helps stabilize these anti-MXenes.

The Metallicity of Anti-MXenes. The semiconducting nature of 1H MoS_2 is due to the full occupation of Mo $4d_{z^2}$ orbitals, which exposes the band gap between Mo $4d_{z^2}$ and $4d_{xy}/d_{x^2-y^2}$ to the Fermi level.[88] Altering the coordination environment of the Mo atom could lead to the rearrangement of d orbitals, making the enhancement of electrical conductivity possible. For example, a semiconducting to metallic electronic property change for MoS_2 is confirmed, when the prismatic D_{3h}-MoS_6 coordination environment of Mo in 1H phase changes to the octahedral O_h-MoS_6 in the 1T phase.[89,90] Here for anti-MXenes, the transition metal atoms are all tetra-coordinated. As revealed by electronic band structures and density of states calculations, the tetrahedral coordination, as well as the increased M/X ratio compared with MoS_2, renders metallicity for these anti-MXenes (Figure S7).

Taking CoB and CuS as examples, their metallic electronic properties are indicated by the crossing of the Fermi level through the electronic bands. For CoB (Figure 4a), the

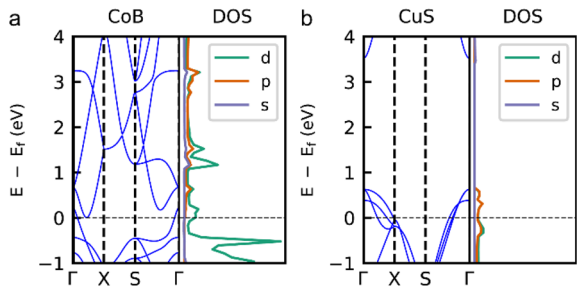

Figure 4. Band structures and projected density of states for (a) CoB and (b) CuS. Fermi level is set at 0 eV, as indicated by the horizontal dash line.

electronic bands around the Fermi level are mainly contributed by the d orbitals of metal Co. A similar feature is found for other 19 anti-MXenes, namely CoAs, CoP, CoS, CoSe, CoSi, CrAs, FeB, FeSe, IrB, IrP, MnAs, MnP, NiS, OsP, RhAs, RhP, RuAs, RuP, and TcSi. However, for CuS (Figure 4b), IrGe, IrSi, and PtSi, both the p orbitals of nonmetal elements and the

https://dx.doi.org/10.1021/acsnano.0c08429
ACS Nano 2021, 15, 6233−6242

d orbitals of metal elements contribute to the bands around the Fermi level. Since the Perdew−Burke−Ernzerhof (PBE) functional tends to underestimate the band gap of semiconductors, one may wonder whether CoB and CuS can become semiconductors if a hybrid functional is applied. Using the HSE06 hybrid functional,[91] we found the electronic band structures of CoB and CuS maintain their metallic properties (Figure S8). As a short remark, the HSE06 hybrid functional results remain qualitatively similar to that of the PBE functional. Such a finding was also reported by Zhang *et al.*,[92] who revealed that the PBE and HSE06 functionals show similar electronic band structures for metallic T6-carbon. The metallicity of these anti-MXenes endows them with a potential application as candidate catalysts for HER and as electrode materials for metal-ion batteries,[93,94] since the conductivity can improve the efficiency and avoid energy loss caused by resistance in the electrochemical process.[62]

Catalytic Performance toward HER. To demonstrate the capability of anti-MXenes as electrocatalysts, we evaluated their catalytic performance toward HER at different levels of H coverage. Computational screening for the optimal electrocatalyst is usually based on the descriptor parameter determined by the adsorption Gibbs free energy of hydrogen atom (ΔG_{*H}).[95] A catalyst is promising only if ΔG_{*H} is close to zero. In this work, the criterion for a promising catalyst is set as $|\Delta G_{*H}| < 0.10$ eV, because the benchmark reference, Pt electrocatalyst, has a theoretical ΔG_{*H} value of −0.09 eV at a H coverage of 25.00%.[95]

A typical anti-MXene, for example, CrAs, has three adsorption sites for a H atom on one side of the surface, while CoB, FeB, and IrB all have six adsorption sites (denoted as "×" in Figure 5 and Figure S9). Different adsorption sites

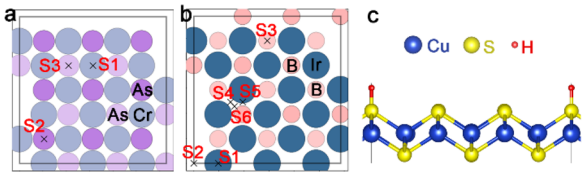

Figure 5. Active sites of anti-MXenes for HER. Possible active sites (×) of H adsorption on (a) CrAs and (b) IrB, both from the same side of the materials. (c) Optimized geometry for H on CuS at a low H coverage.

lead to different adsorption configurations and free energies ΔG_{*H}. In the following analysis, the energetically most favorable configuration for each material was adopted to calculate ΔG_{*H}. We also examined the effect of H coverage. To mimic a low H coverage on the catalyst surface, a 3 × 3 × 1 supercell was used. Since a 3 × 3 × 1 supercell of anti-MXene contains nine nonmetal atoms on the top atomic layer, the H coverage (θ) is calculated to be 1/9 = 11.11%. At this low θ, H prefers to be adsorbed atop of the nonmetal atom in the basal plane for most anti-MXenes (Figure 5c and Table S6), except for MnAs, FeB, RuAs, and TcSi (Figure S10).

As far as the ΔG_{*H} values are concerned, these anti-MXenes exhibit versatile behaviors toward H adsorption (Figure 6a). Ten anti-MXenes (from FeSe to MnP) do not bind H without applied bias due to the positive value of ΔG_{*H}. In comparison, six anti-MXenes, including RuAs, RhP, CoP, CoB, CuS, and RuP, bind H weakly due to the almost neutral ΔG_{*H}, while the remaining eight anti-MXenes (from FeB to IrSi) bind H

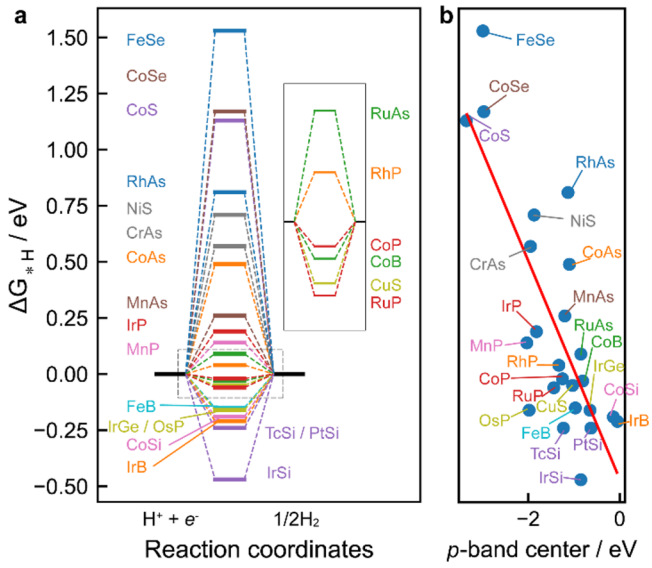

Figure 6. HER performance of 24 stable anti-MXenes. (a) Adsorption free energy for H atom on anti-MXenes. The inset shows potential electrocatalysts within the criterion $|\Delta G_{*H}| < 0.10$ eV. (b) ΔG_{*H} as a function of *p*-band center.

strongly. The adsorption free energy is mainly controlled by the nonmetal element X that binds H. A rough rule of thumb is that X with a higher atomic number has more electrons in *p* orbitals, leading to a lower band center of *p* orbitals (*p*-band center). The *p*-band center, ε_p, is calculated as $\varepsilon_p = \int_{-\infty}^{\infty} x\rho(x)dx / \int_{-\infty}^{\infty} \rho(x)dx$, where x is the energy level with respect to the Fermi level, and $\rho(x)$ is the density of states of *p* orbitals.[96] When interacting with H, a lower ε_p results in a weak adsorption, and a higher ε_p results in a stronger adsorption. Such a rationalization is confirmed by the plot of adsorption energy *vs* ε_p (Figure 6b). The ε_p of CoS is the lowest, corresponding to an unfavorable H adsorption free energy; in contrast, IrB and CoSi feature high *p*-band centers, thus, they can adsorb H atom with large strengths. Encouragingly, CoP, CoB, and CuS are excellent HER electrocatalysts under this H coverage, evidenced by the calculated nearly zero ΔG_{*H} values (−0.02, −0.03, and −0.05 eV, respectively) and their noble-metal-free compositions.

Since the H coverage also affects ΔG_{*H},[95] more electrocatalysts could be discovered at high H coverage. Thus, we selected CoP, CoB, CuS, FeB, and CoSi to study their catalytic performance at higher H coverage because of their negative and close to zero ΔG_{*H} values at θ = 11.11% and their low cost, while excluding IrSi, PtSi, TcSi, IrB, IrGe, OsP, RuP, RhP, and RuAs, since the component transition metals are either precious or radioactive. To simulate the increased H coverage, we constructed and optimized 2 × 2 × 1 (25.00% H coverage), $\sqrt{2} \times \sqrt{2} \times 1$ supercell (50.00% H coverage), and 1× 1 × 1 primitive cell (100.00% H coverage) of CoP, CoB, CuS, FeB, and CoSi monolayers (Figure S11).

According to our computations, with H coverage, θ increased from low (11.11%) to medium (50.00%), and the ΔG_{*H} of CoP, CoB, CuS, FeB, and CoSi become less negative or even positive; with θ increased further to full coverage (100.00%), the ΔG_{*H} of CoB drops, while the rest maintain the increasing trend (Figure 7). The peculiar behavior of CoB can be ascribed to the electron-deficient B atoms. It is found that CoB and CoP can boost the HER at low H coverage,

https://dx.doi.org/10.1021/acsnano.0c08429
ACS Nano 2021, 15, 6233−6242

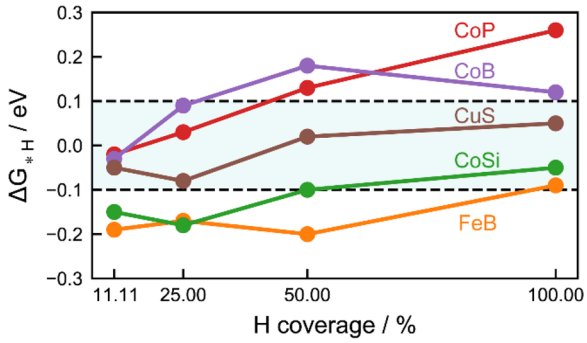

Figure 7. HER performance evaluated by ΔG_{*H} under various H coverages and strains. Shaded region indicates the HER catalyst activity criterion ($|\Delta G_{*H}| < 0.10$ eV).

while CoSi and FeB show promise for HER only with a H coverage close to 100.00%. In comparison, the ΔG_{*H} values of CuS satisfy the criterion of $|\Delta G_{*H}| < 0.10$ eV in the whole range of H coverage. The ΔG_{*H} values of CuS are −0.08 eV (θ = 25.00%), 0.02 eV (θ = 50.00%), and 0.05 eV (θ = 100.00%), respectively. Thus, CuS is determined to be an effective electrocatalyst to HER at the whole range of H coverage. Additionally, the active sites are tetra-coordinating sulfur atoms at the basal plane, presenting a high density of available active sites of 1.33×10^{19} site/m^2 if only one side of the surfaces is considered.

Performance as Anode Materials for LIBs. The development of LIBs is often hindered due to the limited choice of anode materials.[97] The predicted anti-MXenes in this work have rather similar morphology to FeSe monolayer, which was proposed by Lv *et al.* as a promising LIB anode material due to its low Li diffusion barrier (0.16 eV) and high capacity (658 mA h g^{-1}).[94] The high specific surface area and metallic feature of the predicted anti-MXenes also encouraged us to examine their capability as anode materials for LIBs. The CoB and FeB anti-MXenes are expected to be good candidates because their molar masses are much smaller among the 24 anti-MXenes (Table S7), which indicates the possibility of a high capacity. Below we exemplify the application of anti-MXenes in LIBs with CoB and FeB.

Similar to the adsorption of hydrogen atoms, there are six sites to adsorb lithium atoms on the surface of CoB and FeB monolayer (Figure S9). The Li adsorption energies on these sites of CoB (FeB) are in the range of −1.58 (−1.62) to −0.69 (−0.87) eV, and the binding strength follows the order of S3 > S5 > S1 > S4 > S6 > S2 for both CoB and FeB (Figure S12). Using the climbing image nudged elastic band (CI-NEB) method,[98] we investigated the Li diffusion from one energetically most favorable adsorption site (S3) to its neighboring most stable site (S3). Along the identified S3−S1−S3 pathway (S3−S1−S3, Figure 8a), the transition state coincides with the configuration of Li adsorbed on the S1 site, and the energy barrier is 0.41 (0.42) eV for CoB (FeB) (Figure 8b), which is slightly higher that on graphene (0.33 eV) and is within the range of some commercially available anode materials such as TiO_2 (0.35−0.65 eV).[97,99]

By gradually adding layers of Li atoms to the surface, the theoretical capacity of CoB (FeB) for Li storage can be determined (Figure 8c). The first layer of Li atoms (closet to the surface) are all adsorbed on the energetically most favorable S3 sites, followed by the second layer of Li atoms adsorbed over the S2 sites, and the third and fourth layers of Li

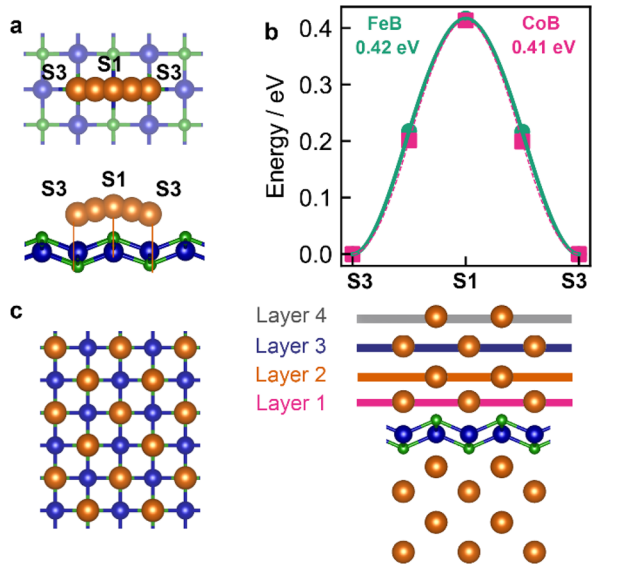

Figure 8. Diffusion path of Li on CoB and geometry of $CoBLi_4$. (a) Scheme of the diffusion path S3−S1−S3. (b) The Li diffusion energy trajectory along the S3−S1−S3 path for CoB and FeB. (c) Optimized geometry of $CoBLi_4$ with four layers of Li atoms adsorbed at each side. $CoBLi_4$ contains the substructures of $CoBLi_1$ and $CoBLi_3$.

atoms are further away from the surface and are above the S3 and S2 sites, respectively. When both sides of the CoB (FeB) surface are adsorbed by layers of Li atoms, the average Li adsorption energies for one-, three-, and four-layer Li adsorptions are −1.38 (−2.24), −0.48 (−0.77), and −0.35 (−0.57) eV/Li atom, respectively (Figure S13). Thus, four layers of Li atoms can be stably adsorbed on the CoB (FeB) monolayer, which corresponds to a theoretical capacity of 1099.44 (1135.77) mA h g^{-1}, much higher than the commercial graphite anode (372 mA h g^{-1}).[100] The calculated open circuit voltage (OCV) values for CoB (FeB) are in the range of 0.35−1.38 (0.57−2.24) V *vs* Li$^+$/Li depending on the number of layers of Li atoms, which are higher than that of graphite (0.11 V),[101] indicating that the formation of Li dendrites can potentially be prevented and the battery safety would thus be improved.[102] On the other hand, a small OCV is demanded for a higher voltage output. Therefore, CoB beats FeB due to its relative smaller OCV and smaller diffusion energy barrier. Moreover, the metallicity of the CoB monolayer can be well maintained after lithiation at different degrees (Figure S14). All these characteristics suggest that the CoB monolayer is a promising anode material for LIBs.

CONCLUSIONS

Taking advantage of the Materials Project database and by means of density functional theory (DFT) computations, we have computationally predicted 79 FeSe-like anti-MXenes from non-van der Waals bulk materials and explored their potential for electrochemical applications. We named these 2DTMCs as anti-MXenes since they have a stacking sequence of atomic layers opposite to that of the extensively studied MXenes. For simplicity, they can be alternatively called XMenes, which can be extracted from their precursor bulk XAM phase. Out of the 79 anti-MXenes, we have identified 24 structures which have good thermodynamic, dynamic, mechanical, and thermal stabilities. Their intrinsic metallicity

https://dx.doi.org/10.1021/acsnano.0c08429
ACS Nano 2021, 15, 6233−6242

and active basal plane endow them with advantages for electrochemical applications in addition to opportunities for unconventional superconductivity.[49−51,108] Five noble-metal-free anti-MXenes, namely CoP, CoB, CoSi, FeB, and CuS monolayers, show good catalytic activity toward hydrogen reduction reactions at different levels of H coverage. In comparison, the CuS catalyst shows promise for HER at both low and high H coverages. Moreover, CoB is a promising anode material for LIBs, as indicated by its low Li diffusion barrier, suitable OCV, and very high Li capacity. Overall, this work will promote "computational exfoliation" of many other 2D materials from non-van der Waals bulks and calls for further experimental explorations of anti-MXenes for even more electrochemical applications.

METHODS

To establish our own material library of anti-MXenes, the *query* method from the Pymatgen package was used to acquire XAM phases with the specific *I*4/*mmm* symmetry from the Materials Project database.[70] These XAM phases were grouped according to the X elements. Then, the structural parameters of these XAM phases were scanned by in-house python scripts to construct potential anti-MXenes by removing the A elements. Simultaneously, these anti-MXenes were compared to each other to avoid repetitions. For the python scripts and library of anti-MXenes, visit the link https://github.com/gvenus/Anti-MXenes. The *adsorption* module of the Pymatgen code was applied to find all adsorption sites of the anti-MXenes for the adsorption of hydrogen and lithium atoms.

All computations, such as geometry optimizations, stability evaluations, and property analysis, were performed at the level of DFT *via* the Vienna *ab initio* simulation package (VASP).[103,104] The spin-polarization was switched on, except for materials that were confirmed to be spin restricted. Unless otherwise noted, the generalized gradient approximation in the form of Perdew−Burke−Ernzerhof was used to describe the exchange−correlation for electrons.[105] The lattice constant along *z* direction of all 2D materials was fixed to 20 Å to avoid the interactions from adjacent periodic images for all kinds of calculations. During the structural relaxations, a high-energy cutoff of 700 eV was adopted, along with a fine energy convergence criterion of 10^{-8} eV and a force convergence criterion of 0.01 eV/Å. The corresponding *k*-point grid was 12 × 12 × 1. Phonon spectra were calculated using PHONOPY code,[106] where the force constants were obtained by means of density functional perturbation theory. Here, the energy cutoff, energy convergence, and force convergence were the same as those of structural relaxations. *Ab initio* molecular dynamics (AIMD) simulations were carried out in the canonical (NVT) ensemble using a Nosé thermostat,[107] and the temperature was set as 374 K, with an energy cutoff of 450 eV and an energy convergence of 2 × 10^{-5} eV. For Phonon and AIMD calculations, the 3 × 3 × 1 supercell of material was adopted, and the *k*-point grid was correspondingly set to 4 × 4 × 1. Elastic constants were obtained by the VASPKIT code,[71] with the energy cutoff, energy convergence, and force convergence the same as those of structural relaxations and phonon calculations. A *k*-point grid of 12 × 12 × 1 was adopted for this calculation using the primitive cells from the structural relaxations. Details for the evaluation of HER performance and the performance as LIB anode materials are given in the Supporting Information.

ASSOCIATED CONTENT

Supporting Information

The Supporting Information is available free of charge at https://pubs.acs.org/doi/10.1021/acsnano.0c08429.

Computational methods to evaluate the performance of anti-MXenes as electrocatalysts for HER and as anode materials for LIBs; optimized lattice parameters, cohesive energies, phonon spectra, AIMD simulation results, and elastic constants of anti-MXenes; charge density difference and electron localization function plots, band structures, and density of states of 24 stable anti-MXenes; adsorption sites, energies, and structures of hydrogen and lithium on selected anti-MXenes (PDF)

AUTHOR INFORMATION

Corresponding Authors

Jingsong Huang − *Center for Nanophase Materials Sciences, Oak Ridge National Laboratory, Oak Ridge, Tennessee 37831, United States;* orcid.org/0000-0001-8993-2506; Email: huangj3@ornl.gov

Zhongfang Chen − *Department of Chemistry, University of Puerto Rico, San Juan, Puerto Rico 00931, United States;* orcid.org/0000-0002-1445-9184; Email: zhongfangchen@gmail.com

Authors

Jinxing Gu − *Department of Chemistry, University of Puerto Rico, San Juan, Puerto Rico 00931, United States;* orcid.org/0000-0003-4805-7017

Ziyuan Zhao − *Department of Chemistry, University of Puerto Rico, San Juan, Puerto Rico 00931, United States*

Bobby G. Sumpter − *Center for Nanophase Materials Sciences, Oak Ridge National Laboratory, Oak Ridge, Tennessee 37831, United States;* orcid.org/0000-0001-6341-0355

Complete contact information is available at: https://pubs.acs.org/10.1021/acsnano.0c08429

Notes

The authors declare no competing financial interest.

ACKNOWLEDGMENTS

This work was financially supported by the NSF Center for the Advancement of Wearable Technologies (grant 1849243) and by NASA (grant no. 80NSSC19M0236). A portion of the calculations used the resources of the Compute and Data Environment for Science (CADES) at ORNL and of the National Energy Research Scientific Computing Center, which are supported by the Office of Science of the U.S. DOE under contract nos. DE-AC05-00OR22750 and DE-AC02-05CH11231, respectively. Some of the work was performed at the Center for Nanophase Materials Sciences, a U.S. DOE Office of Science User Facility. This paper is dedicated to Professor Andreas Hirsch on the occasion of his 60th birthday.

REFERENCES

(1) Maghami, M. R.; Hassani, R.; Gomes, C.; Hizam, H.; Othman, M. L.; Behmanesh, M. Hybrid Energy Management with Respect to a Hydrogen Energy System and Demand Response. *Int. J. Hydrogen Energy* **2020**, *45*, 1499−1509.

(2) Stamenkovic, V. R.; Strmcnik, D.; Lopes, P. P.; Markovic, N. M. Energy and Fuels from Electrochemical Interfaces. *Nat. Mater.* **2017**, *16*, 57−69.

(3) Turner, J. A. Sustainable Hydrogen Production. *Science* **2004**, *305*, 972−974.

(4) Feng, W.; Pang, W.; Xu, Y.; Guo, A.; Gao, X.; Qiu, X.; Chen, W. Transition Metal Selenides for Electrocatalytic Hydrogen Evolution Reaction. *ChemElectroChem* **2020**, *7*, 31−54.

(5) Hasani, A.; Tekalgne, M.; Le, Q. V.; Jang, H. W.; Kim, S. Y. Two-Dimensional Materials As Catalysts for Solar Fuels: Hydrogen Evolution Reaction and CO_2 Reduction. *J. Mater. Chem. A* **2019**, *7*, 430−454.
(6) Yu, P.; Wang, F.; Shifa, T. A.; Zhan, X.; Lou, X.; Xia, F.; He, J. Earth Abundant Materials beyond Transition Metal Dichalcogenides: A Focus on Electrocatalyzing Hydrogen Evolution Reaction. *Nano Energy* **2019**, *58*, 244−276.
(7) Zheng, Y.; Jiao, Y.; Zhu, Y.; Li, L. H.; Han, Y.; Chen, Y.; Du, A.; Jaroniec, M.; Qiao, S. Z. Hydrogen Evolution by a Metal-Free Electrocatalyst. *Nat. Commun.* **2014**, *5*, 3783.
(8) Zhu, K.; Li, C.; Jing, Z.; Liu, X.; He, Y.; Lv, X.; Wang, Y.; Liu, K. Two-Dimensional Transition-Metal Dichalcogenides for Electrochemical Hydrogen Evolution Reaction. *FlatChem.* **2019**, *18*, 100140.
(9) Zheng, Y.; Li, X.; Pi, C.; Song, H.; Gao, B.; Chu, P. K.; Huo, K. Recent Advances of Two-Dimensional Transition Metal Nitrides for Energy Storage and Conversion Applications. *FlatChem.* **2020**, *19*, 100149.
(10) Naguib, M.; Mashtalir, O.; Carle, J.; Presser, V.; Lu, J.; Hultman, L.; Gogotsi, Y.; Barsoum, M. W. Two-Dimensional Transition Metal Carbides. *ACS Nano* **2012**, *6*, 1322−1331.
(11) Cheng, Y.-W.; Dai, J.-H.; Zhang, Y.-M.; Song, Y. Two-Dimensional, Ordered, Double Transition Metal Carbides (MXenes): A New Family of Promising Catalysts for the Hydrogen Evolution Reaction. *J. Phys. Chem. C* **2018**, *122*, 28113−28122.
(12) Handoko, A. D.; Fredrickson, K. D.; Anasori, B.; Convey, K. W.; Johnson, L. R.; Gogotsi, Y.; Vojvodic, A.; Seh, Z. W. Tuning the Basal Plane Functionalization of Two-Dimensional Metal Carbides (MXenes) to Control Hydrogen Evolution Activity. *ACS Appl. Energy Mater.* **2018**, *1*, 173−180.
(13) Yuan, S.; Pang, S.-Y.; Hao, J. 2D Transition Metal Dichalcogenides, Carbides, Nitrides, and Their Applications in Supercapacitors and Electrocatalytic Hydrogen Evolution Reaction. *Appl. Phys. Rev.* **2020**, *7*, 021304.
(14) Xie, J.; Yang, X.; Xie, Y. Defect Engineering in Two-Dimensional Electrocatalysts for Hydrogen Evolution. *Nanoscale* **2020**, *12*, 4283−4294.
(15) Zhang, H. Ultrathin Two-Dimensional Nanomaterials. *ACS Nano* **2015**, *9*, 9451−9469.
(16) Chia, X.; Pumera, M. Characteristics and Performance of Two-Dimensional Materials for Electrocatalysis. *Nat. Catal.* **2018**, *1*, 909−921.
(17) Di, J.; Yan, C.; Handoko, A. D.; Seh, Z. W.; Li, H.; Liu, Z. Ultrathin Two-Dimensional Materials for Photo- and Electrocatalytic Hydrogen Evolution. *Mater. Today* **2018**, *21*, 749−770.
(18) Zhang, H.; Lv, R. Defect Engineering of Two-Dimensional Materials for Efficient Electrocatalysis. *J. Materiomics* **2018**, *4*, 95−107.
(19) Wang, X.; Chen, Y.; Zheng, B.; Qi, F.; He, J.; Li, Q.; Li, P.; Zhang, W. Graphene-Like WSe_2 Nanosheets for Efficient and Stable Hydrogen Evolution. *J. Alloys Compd.* **2017**, *691*, 698−704.
(20) Pan, J.; Wang, R.; Xu, X.; Hu, J.; Ma, L. Transition Metal Doping Activated Basal-Plane Catalytic Activity of Two-Dimensional 1T'-ReS_2 for Hydrogen Evolution Reaction: A First-Principles Calculation Study. *Nanoscale* **2019**, *11*, 10402−10409.
(21) Chirdon, D. N.; Wu, Y. Hydrogen Evolution: Not Living on the Edge. *Nat. Energy* **2017**, *2*, 17132.
(22) Kwon, H.; Bae, D.; Jun, H.; Ji, B.; Won, D.; Lee, J.-H.; Son, Y.-W.; Yang, H.; Cho, S. Basal-Plane Catalytic Activity of Layered Metallic Transition Metal Ditellurides for the Hydrogen Evolution Reaction. *Appl. Sci.* **2020**, *10*, 3087.
(23) Wu, H.-H.; Huang, H.; Zhong, J.; Yu, S.; Zhang, Q.; Zeng, X. C. Monolayer Triphosphates MP_3 (M = Sn, Ge) with Excellent Basal Catalytic Activity for Hydrogen Evolution Reaction. *Nanoscale* **2019**, *11*, 12210−12219.
(24) Hu, T.; Tai, G.; Wu, Z.; Wang, R.; Hou, C.; Sheng, L. Ultrathin Molybdenum Phosphide Films as High-Efficiency Electrocatalysts for Hydrogen Evolution Reaction. *Mater. Res. Express* **2019**, *6*, 016418.
(25) Liu, Q.; Xing, J.; Jiang, Z.; Jiang, X.; Wang, Y.; Zhao, J. 2D Tetragonal Transition-Metal Phosphides: An Ideal Platform to Screen Metal Shrouded Crystals for Multifunctional Applications. *Nanoscale* **2020**, *12*, 6776−6784.
(26) Seh, Z. W.; Fredrickson, K. D.; Anasori, B.; Kibsgaard, J.; Strickler, A. L.; Lukatskaya, M. R.; Gogotsi, Y.; Jaramillo, T. F.; Vojvodic, A. Two-Dimensional Molybdenum Carbide (MXene) as an Efficient Electrocatalyst for Hydrogen Evolution. *ACS Energy Lett.* **2016**, *1*, 589−594.
(27) Zeng, M.; Chen, Y.; Li, J.; Xue, H.; Mendes, R. G.; Liu, J.; Zhang, T.; Rümmeli, M. H.; Fu, L. 2D WC Single Crystal Embedded in Graphene for Enhancing Hydrogen Evolution Reaction. *Nano Energy* **2017**, *33*, 356−362.
(28) Yu, Y.; Zhou, J.; Sun, Z. Novel 2D Transition-Metal Carbides: Ultrahigh Performance Electrocatalysts for Overall Water Splitting and Oxygen Reduction. *Adv. Funct. Mater.* **2020**, *30*, 2000570.
(29) Wang, A.; Shen, L.; Zhao, M.; Wang, J.; Zhou, W.; Li, W.; Feng, Y.; Liu, H. Tungsten Boride: A 2D Multiple Dirac Semimetal for the Hydrogen Evolution Reaction. *J. Mater. Chem. C* **2019**, *7*, 8868−8873.
(30) Wang, X.; Tai, G.; Wu, Z.; Hu, T.; Wang, R. Ultrathin Molybdenum Boride Films for Highly Efficient Catalysis of the Hydrogen Evolution Reaction. *J. Mater. Chem. A* **2017**, *5*, 23471−23475.
(31) Jaramillo, T. F.; Jørgensen, K. P.; Bonde, J.; Nielsen, J. H.; Horch, S.; Chorkendorff, I. Identification of Active Edge Sites for Electrochemical H_2 Evolution from MoS_2 Nanocatalysts. *Science* **2007**, *317*, 100−102.
(32) Kumar, A.; Ahluwalia, P. K. A First Principle Comparative Study of Electronic and Optical Properties of 1H-MoS_2 and 2H-MoS_2. *Mater. Chem. Phys.* **2012**, *135*, 755−761.
(33) Hinnemann, B.; Moses, P. G.; Bonde, J.; Jørgensen, K. P.; Nielsen, J. H.; Horch, S.; Chorkendorff, I.; Nørskov, J. K. Biomimetic Hydrogen Evolution: MoS_2 Nanoparticles as Catalyst for Hydrogen Evolution. *J. Am. Chem. Soc.* **2005**, *127*, 5308−5309.
(34) Wang, C.; Huang, J.; Chen, J.; Xi, Z.; Deng, X. Progress in Electrocatalytic Hydrogen Evolution Based on Monolayer Molybdenum Disulfide. *Front. Chem.* **2019**, *7*, 131.
(35) Tsai, C.; Chan, K.; Abild-Pedersen, F.; Nørskov, J. K. Active Edge Sites in $MoSe_2$ and WSe_2 Catalysts for the Hydrogen Evolution Reaction: A Density Functional Study. *Phys. Chem. Chem. Phys.* **2014**, *16*, 13156−13164.
(36) Guo, X.; Gu, J.; Hu, X.; Zhang, S.; Chen, Z.; Huang, S. Coordination Tailoring towards Efficient Single-Atom Catalysts for N_2 Fixation: A Case Study of Iron-Nitrogen-Carbon (Fe@N-C) Systems. *Catal. Today* **2020**, *350*, 91−99.
(37) Wang, D.; Ao, C.; Liu, X.; Fang, S.; Lin, Y.; Liu, W.; Zhang, W.; Zheng, X.; Zhang, L.; Yao, T. Coordination-Engineered Cu-N_x Single-Site Catalyst for Enhancing Oxygen Reduction Reaction. *ACS Appl. Energy Mater.* **2019**, *2*, 6497−6504.
(38) Li, X. D.; Wu, S. Q.; Zhu, Z. Z. Band Gap Control and Transformation of Monolayer-MoS_2-Based Hetero-Bilayers. *J. Mater. Chem. C* **2015**, *3*, 9403−9411.
(39) Gao, G.; O'Mullane, A. P.; Du, A. 2D MXenes: A New Family of Promising Catalysts for the Hydrogen Evolution Reaction. *ACS Catal.* **2017**, *7*, 494−500.
(40) Voiry, D.; Yang, J.; Chhowalla, M. Recent Strategies for Improving the Catalytic Activity of 2D TMD Nanosheets toward the Hydrogen Evolution Reaction. *Adv. Mater.* **2016**, *28*, 6197−6206.
(41) Park, S.; Park, J.; Abroshan, H.; Zhang, L.; Kim, J. K.; Zhang, J.; Guo, J.; Siahrostami, S.; Zheng, X. Enhancing Catalytic Activity of MoS_2 Basal Plane S-Vacancy by Co Cluster Addition. *ACS Energy Lett.* **2018**, *3*, 2685−2693.
(42) Tsai, C.; Li, H.; Park, S.; Park, J.; Han, H. S.; Nørskov, J. K.; Zheng, X.; Abild-Pedersen, F. Electrochemical Generation of Sulfur Vacancies in the Basal Plane of MoS_2 for Hydrogen Evolution. *Nat. Commun.* **2017**, *8*, 15113.
(43) Wang, C.; Lu, H.; Tang, K.; Mao, Z.; Li, Q.; Wang, X.; Yan, C. Atom Removal on the Basal Plane of Layered MoS_2 Leading to

https://dx.doi.org/10.1021/acsnano.0c08429
ACS Nano 2021, 15, 6233−6242

Extraordinarily Enhanced Electrocatalytic Performance. *Electrochim. Acta* **2020**, *336*, 135740.
(44) Wu, W.; Niu, C.; Wei, C.; Jia, Y.; Li, C.; Xu, Q. Activation of MoS_2 Basal Planes for Hydrogen Evolution by Zinc. *Angew. Chem., Int. Ed.* **2019**, *58*, 2029−2033.
(45) Ouyang, Y.; Ling, C.; Chen, Q.; Wang, Z.; Shi, L.; Wang, J. Activating Inert Basal Planes of MoS_2 for Hydrogen Evolution Reaction through the Formation of Different Intrinsic Defects. *Chem. Mater.* **2016**, *28*, 4390−4396.
(46) Li, G.; Zhang, D.; Qiao, Q.; Yu, Y.; Peterson, D.; Zafar, A.; Kumar, R.; Curtarolo, S.; Hunte, F.; Shannon, S.; Zhu, Y.; Yang, W.; Cao, L. All the Catalytic Active Sites of MoS_2 for Hydrogen Evolution. *J. Am. Chem. Soc.* **2016**, *138*, 16632−16638.
(47) Wu, C.; Li, D.; Ding, S.; Rehman, Z. U.; Liu, Q.; Chen, S.; Zhang, B.; Song, L. Monoatomic Platinum-Anchored Metallic MoS_2: Correlation between Surface Dopant and Hydrogen Evolution. *J. Phys. Chem. Lett.* **2019**, *10*, 6081−6087.
(48) Yang, T.; Zhou, J.; Song, T. T.; Shen, L.; Feng, Y. P.; Yang, M. High-Throughput Identification of Exfoliable Two-Dimensional Materials with Active Basal Planes for Hydrogen Evolution. *ACS Energy Lett.* **2020**, *5*, 2313−2321.
(49) Ge, J.-F.; Liu, Z.-L.; Liu, C.; Gao, C.-L.; Qian, D.; Xue, Q.-K.; Liu, Y.; Jia, J.-F. Superconductivity above 100 K in Single-Layer FeSe Films on Doped $SrTiO_3$. *Nat. Mater.* **2015**, *14*, 285−289.
(50) Luo, C. W.; Wu, I. H.; Cheng, P. C.; Lin, J. Y.; Wu, K. H.; Uen, T. M.; Juang, J. Y.; Kobayashi, T.; Chareev, D. A.; Volkova, O. S.; Vasiliev, A. N. Quasiparticle Dynamics and Phonon Softening in FeSe Superconductors. *Phys. Rev. Lett.* **2012**, *108*, 257006.
(51) Zhou, Y.; Miao, L.; Wang, P.; Zhu, F. F.; Jiang, W. X.; Jiang, S. W.; Zhang, Y.; Lei, B.; Chen, X. H.; Ding, H. F.; Zheng, H.; Zhang, W. T.; Jia, J. F.; Qian, D.; Wu, D. Antiferromagnetic Order in Epitaxial FeSe Films on $SrTiO_3$. *Phys. Rev. Lett.* **2018**, *120*, 097001.
(52) Li, W.; Ding, H.; Li, Z.; Deng, P.; Chang, K.; He, K.; Ji, S.; Wang, L.; Ma, X.; Hu, J.-P.; Chen, X.; Xue, Q. K. KFe_2Se_2 is the Parent Compound of K-Doped Iron Selenide Superconductors. *Phys. Rev. Lett.* **2012**, *109*, 057003.
(53) Guo, J.; Jin, S.; Wang, G.; Wang, S.; Zhu, K.; Zhou, T.; He, M.; Chen, X. Superconductivity in the Iron Selenide $K_xFe_2Se_2$ ($0 \leq x \leq 1.0$). *Phys. Rev. B: Condens. Matter Mater. Phys.* **2010**, *82*, No. 180520.
(54) Balan, A. P.; Radhakrishnan, S.; Woellner, C. F.; Sinha, S. K.; Deng, L.; de los Reyes, C.; Rao, B. M.; Paulose, M.; Neupane, R.; Apte, A.; Kochat, V.; Vajtai, R.; Harutyunyan, A. R.; Chu, C. W.; Costin, G.; Galvao, D. S.; Martí, A. A.; van Aken, P. A.; Varghese, O. K.; Tiwary, C.; et al. Exfoliation of a Non-van der Waals Material from Iron Ore Hematite. *Nat. Nanotechnol.* **2018**, *13*, 602−609.
(55) Du, Z.; Yang, S.; Li, S.; Lou, J.; Zhang, S.; Wang, S.; Li, B.; Gong, Y.; Song, L.; Zou, X.; Ajayan, P. M. Conversion of Non-van der Waals Solids to 2D Transition-Metal Chalcogenides. *Nature* **2020**, *577*, 492−496.
(56) Naguib, M.; Mochalin, V. N.; Barsoum, M. W.; Gogotsi, Y. 25th Anniversary Article: MXenes: A New Family of Two-Dimensional Materials. *Adv. Mater.* **2014**, *26*, 992−1005.
(57) Jiang, W.; Zou, X.; Du, H.; Gan, L.; Xu, C.; Kang, F.; Duan, W.; Li, J. Universal Descriptor for Large-Scale Screening of High-Performance MXene-Based Materials for Energy Storage and Conversion. *Chem. Mater.* **2018**, *30*, 2687−2693.
(58) Chia, X.; Ambrosi, A.; Sofer, Z.; Luxa, J.; Sedmidubský, D.; Pumera, M. Anti-MoS_2 Nanostructures: Tl_2S and Its Electrochemical and Electronic Properties. *ACS Nano* **2016**, *10*, 112−123.
(59) Singh, A. K.; Mathew, K.; Zhuang, H. L.; Hennig, R. G. Computational Screening of 2D Materials for Photocatalysis. *J. Phys. Chem. Lett.* **2015**, *6*, 1087−1098.
(60) Oganov, A. R.; Pickard, C. J.; Zhu, Q.; Needs, R. J. Structure Prediction Drives Materials Discovery. *Nat. Rev. Mater.* **2019**, *4*, 331−348.
(61) Choudhary, K.; Garrity, K.; Tavazza, F. Data-Driven Discovery of 3D and 2D Thermoelectric Materials. *J. Phys.: Condens. Matter* **2020**, *32*, 475501.
(62) Yao, S.; Zhang, X.; Chen, A.; Zhang, Z.; Jiao, M.; Zhou, Z. Algorithm Screening to Accelerate Discovery of 2D Metal-Free Electrocatalysts for Hydrogen Evolution Reaction. *J. Mater. Chem. A* **2019**, *7*, 19290−19296.
(63) Lebègue, S.; Björkman, T.; Klintenberg, M.; Nieminen, R. M.; Eriksson, O. Two-Dimensional Materials from Data Filtering and *ab Initio* Calculations. *Phys. Rev. X* **2013**, *3*, 031002.
(64) Revard, B. C.; Tipton, W. W.; Yesypenko, A.; Hennig, R. G. Grand-Canonical Evolutionary Algorithm for the Prediction of Two-Dimensional Materials. *Phys. Rev. B: Condens. Matter Mater. Phys.* **2016**, *93*, 054117.
(65) Ashton, M.; Paul, J.; Sinnott, S. B.; Hennig, R. G. Topology-Scaling Identification of Layered Solids and Stable Exfoliated 2D Materials. *Phys. Rev. Lett.* **2017**, *118*, 106101.
(66) Choudhary, K.; Kalish, I.; Beams, R.; Tavazza, F. High-Throughput Identification and Characterization of Two-Dimensional Materials Using Density Functional Theory. *Sci. Rep.* **2017**, *7*, 5179.
(67) Haastrup, S.; Strange, M.; Pandey, M.; Deilmann, T.; Schmidt, P. S.; Hinsche, N. F.; Gjerding, M. N.; Torelli, D.; Larsen, P. M.; Riis-Jensen, A. C.; et al. The Computational 2D Materials Database: High-Throughput Modeling and Discovery of Atomically Thin Crystals. *2D Mater.* **2018**, *5*, 042002.
(68) Mounet, N.; Gibertini, M.; Schwaller, P.; Campi, D.; Merkys, A.; Marrazzo, A.; Sohier, T.; Castelli, I. E.; Cepellotti, A.; Pizzi, G.; Marzari, N. Two-Dimensional Materials from High-Throughput Computational Exfoliation of Experimentally Known Compounds. *Nat. Nanotechnol.* **2018**, *13*, 246−252.
(69) Zhang, X.; Chen, A.; Zhou, Z. High-Throughput Computational Screening of Layered and Two-Dimensional Materials. *Wiley Interdiscip. Rev.: Comput. Mol. Sci.* **2019**, *9*, No. e1385.
(70) Ong, S. P.; Richards, W. D.; Jain, A.; Hautier, G.; Kocher, M.; Cholia, S.; Gunter, D.; Chevrier, V. L.; Persson, K. A.; Ceder, G. Python Materials Genomics (PYMATGEN): A Robust, Open-Source Python Library for Materials Analysis. *Comput. Mater. Sci.* **2013**, *68*, 314−319.
(71) Wang, V.; Xu, N.; Liu, J.-C.; Tang, G.; Geng, W.-T. VASPKIT: A Pre- and Post-Processing Program for VASP Code. *arXiv (Materials Science)*, June 25, 2020, 1908.08269, ver. 5. https://arxiv.org/abs/1908.08269v5 (accessed 2020-06-25).
(72) Tuckerman, M. E. *Ab Initio* Molecular Dynamics: Basic Concepts, Current Trends and Novel Applications. *J. Phys.: Condens. Matter* **2002**, *14*, R1297.
(73) Naguib, M.; Kurtoglu, M.; Presser, V.; Lu, J.; Niu, J.; Heon, M.; Hultman, L.; Gogotsi, Y.; Barsoum, M. W. Two-Dimensional Nanocrystals Produced by Exfoliation of Ti_3AlC_2. *Adv. Mater.* **2011**, *23*, 4248−4253.
(74) Zhou, J.; Lin, J.; Huang, X.; Zhou, Y.; Chen, Y.; Xia, J.; Wang, H.; Xie, Y.; Yu, H.; Lei, J.; Wu, D.; Liu, F.; Fu, Q.; Zeng, Q.; Hsu, C. H.; Yang, C.; Lu, Y.; Yu, T.; Shen, Z.; Lin, H.; et al. A Library of Atomically Thin Metal Chalcogenides. *Nature* **2018**, *556*, 355−359.
(75) Wang, B.; Zhang, Y.; Ma, L.; Wu, Q.; Guo, Y.; Zhang, X.; Wang, J. MnX (X = P, As) Monolayers: A New Type of Two-Dimensional Intrinsic Room Temperature Ferromagnetic Half-Metallic Material with Large Magnetic Anisotropy. *Nanoscale* **2019**, *11*, 4204−4209.
(76) Zhou, J.; Shen, L.; Costa, M. D.; Persson, K. A.; Ong, S. P.; Huck, P.; Lu, Y.; Ma, X.; Chen, Y.; Tang, H.; Feng, Y. P. 2DMatPedia, an Open Computational Database of Two-Dimensional Materials from Top-down and Bottom-up Approaches. *Sci. Data* **2019**, *6*, 86.
(77) Tong, C.-J.; Zhang, H.; Zhang, Y.-N.; Liu, H.; Liu, L.-M. New Manifold Two-Dimensional Single-Layer Structures of Zinc-Blende Compounds. *J. Mater. Chem. A* **2014**, *2*, 17971−17978.
(78) Zhou, J.; Sumpter, B. G.; Kent, P. R. C.; Huang, J. A Novel and Functional Single-Layer Sheet of ZnSe. *ACS Appl. Mater. Interfaces* **2015**, *7*, 1458−1464.
(79) Li, L.; Li, P.; Lu, N.; Dai, J.; Zeng, X. C. Simulation Evidence of Hexagonal-to-Tetragonal ZnSe Structure Transition: A Monolayer Material with a Wide-Range Tunable Direct Bandgap. *Adv. Sci.* **2015**, *2*, 1500290.

https://dx.doi.org/10.1021/acsnano.0c08429
ACS Nano 2021, 15, 6233−6242

(80) Majidi, R. Density Functional Theory Study on Structural and Mechanical Properties of Graphene, T-Graphene, and R-Graphyne. *Theor. Chem. Acc.* **2017**, *136*, 109−116.
(81) Wang, Y.; Li, F.; Li, Y.; Chen, Z. Semi-Metallic Be_5C_2 Monolayer Global Minimum with Quasi-Planar Pentacoordinate Carbons and Negative Poisson's Ratio. *Nat. Commun.* **2016**, *7*, 11488.
(82) Peng, Q.; Liang, C.; Ji, W.; De, S. A Theoretical Analysis of the Effect of the Hydrogenation of Graphene to Graphane on Its Mechanical Properties. *Phys. Chem. Chem. Phys.* **2013**, *15*, 2003−2011.
(83) Cooper, R. C.; Lee, C.; Marianetti, C. A.; Wei, X.; Hone, J.; Kysar, J. W. Nonlinear Elastic Behavior of Two-Dimensional Molybdenum Disulfide. *Phys. Rev. B: Condens. Matter Mater. Phys.* **2013**, *87*, 035423.
(84) Khazaei, M.; Ranjbar, A.; Esfarjani, K.; Bogdanovski, D.; Dronskowski, R.; Yunoki, S. Insights into Exfoliation Possibility of MAX Phases to MXenes. *Phys. Chem. Chem. Phys.* **2018**, *20*, 8579−8592.
(85) Khazaei, M.; Wang, J.; Estili, M.; Ranjbar, A.; Suehara, S.; Arai, M.; Esfarjani, K.; Yunoki, S. Novel MAB Phases and Insights into Their Exfoliation into 2D MBenes. *Nanoscale* **2019**, *11*, 11305−11314.
(86) Champagne, A.; Ricci, F.; Barbier, M.; Ouisse, T.; Magnin, D.; Ryelandt, S.; Pardoen, T.; Hautier, G.; Barsoum, M. W.; Charlier, J.-C. Insights into the Elastic Properties of RE-*i*-Max Phases and Their Potential Exfoliation into Two-Dimensional RE-*i*-MXenes. *Phys. Rev. Mater.* **2020**, *4*, 013604.
(87) Ashton, M.; Mathew, K.; Hennig, R. G.; Sinnott, S. B. Predicted Surface Composition and Thermodynamic Stability of MXenes in Solution. *J. Phys. Chem. C* **2016**, *120*, 3550−3556.
(88) Enyashin, A. N.; Yadgarov, L.; Houben, L.; Popov, I.; Weidenbach, M.; Tenne, R.; Bar-Sadan, M.; Seifert, G. New Route for Stabilization of 1T-WS_2 and MoS_2 Phases. *J. Phys. Chem. C* **2011**, *115*, 24586−24591.
(89) Shi, S.; Sun, Z.; Hu, Y. H. Synthesis, Stabilization and Applications of 2-Dimensional 1T Metallic MoS_2. *J. Mater. Chem. A* **2018**, *6*, 23932−23977.
(90) Gan, X.; Lee, L. Y. S.; Wong, K.-Y.; Lo, T. W.; Ho, K. H.; Lei, D. Y.; Zhao, H. 2H/1T Phase Transition of Multilayer MoS_2 by Electrochemical Incorporation of S Vacancies. *ACS Appl. Energy Mater.* **2018**, *1*, 4754−4765.
(91) Krukau, A. V.; Vydrov, O. A.; Izmaylov, A. F.; Scuseria, G. E. Influence of the Exchange Screening Parameter on the Performance of Screened Hybrid Functionals. *J. Chem. Phys.* **2006**, *125*, 224106.
(92) Zhang, S.; Wang, Q.; Chen, X.; Jena, P. Stable Three-Dimensional Metallic Carbon with Interlocking Hexagons. *Proc. Natl. Acad. Sci. U. S. A.* **2013**, *110*, 18809−18813.
(93) Jiang, Z.; Gu, X.; Wang, L.; Huang, L. First-Principles Study of Intercalation of Alkali Ions in FeSe for Solid-State Batteries. *Chem. Phys. Lett.* **2016**, *659*, 230−233.
(94) Lv, X.; Li, F.; Gong, J.; Gu, J.; Lin, S.; Chen, Z. Metallic FeSe Monolayer as an Anode Material for Li and Non-Li Ion Batteries: A DFT Study. *Phys. Chem. Chem. Phys.* **2020**, *22*, 8902−8912.
(95) Nørskov, J. K.; Bligaard, T.; Logadottir, A.; Kitchin, J. R.; Chen, J. G.; Pandelov, S.; Stimming, U. Trends in the Exchange Current for Hydrogen Evolution. *J. Electrochem. Soc.* **2005**, *152*, J23−J26.
(96) Shi, W.; Fan, K.; Wang, Z. Catalytic Activity for the Hydrogen Evolution Reaction of Edges in Janus Monolayer MoXY (X/Y = S, Se, and Te). *Phys. Chem. Chem. Phys.* **2018**, *20*, 29423−29429.
(97) Dong, Y.; Wei, W.; Lv, X.; Huang, B.; Dai, Y. Semimetallic Si_3C as a High Capacity Anode Material for Advanced Lithium Ion Batteries. *Appl. Surf. Sci.* **2019**, *479*, 519−524.
(98) Henkelman, G.; Uberuaga, B. P.; Jónsson, H. A Climbing Image Nudged Elastic Band Method for Finding Saddle Points and Minimum Energy Paths. *J. Chem. Phys.* **2000**, *113*, 9901−9904.
(99) Tang, Q.; Zhou, Z.; Shen, P. Are MXenes Promising Anode Materials for Li Ion Batteries? Computational Studies on Electronic Properties and Li Storage Capability of Ti_3C_2 and $Ti_3C_2X_2$ (X = F, OH) Monolayer. *J. Am. Chem. Soc.* **2012**, *134*, 16909−16916.
(100) Asenbauer, J.; Eisenmann, T.; Kuenzel, M.; Kazzazi, A.; Chen, Z.; Bresser, D. The Success Story of Graphite as a Lithium-Ion Anode Material-Fundamentals, Remaining Challenges, and Recent Developments Including Silicon (Oxide) Composites. *Sustainable Energy Fuels* **2020**, *4*, 5387−5416.
(101) Jing, Y.; Zhou, Z.; Cabrera, C. R.; Chen, Z. Metallic VS_2 Monolayer: A Promising 2D Anode Material for Lithium Ion Batteries. *J. Phys. Chem. C* **2013**, *117*, 25409−25413.
(102) Yang, Z.; Choi, D.; Kerisit, S.; Rosso, K. M.; Wang, D.; Zhang, J.; Graff, G.; Liu, J. Nanostructures and Lithium Electrochemical Reactivity of Lithium Titanites and Titanium Oxides: A Review. *J. Power Sources* **2009**, *192*, 588−598.
(103) Kresse, G.; Furthmüller, J. Efficiency of *ab-Initio* Total Energy Calculations for Metals and Semiconductors Using a Plane-Wave Basis Set. *Comput. Mater. Sci.* **1996**, *6*, 15−50.
(104) Blöchl, P. E. Projector Augmented-Wave Method. *Phys. Rev. B: Condens. Matter Mater. Phys.* **1994**, *50*, 17953.
(105) Perdew, J. P.; Burke, K.; Ernzerhof, M. Generalized Gradient Approximation Made Simple. *Phys. Rev. Lett.* **1996**, *77*, 3865−3868.
(106) Togo, A.; Tanaka, I. First Principles Phonon Calculations in Materials Science. *Scr. Mater.* **2015**, *108*, 1−5.
(107) Nosé, S. A Unified Formulation of the Constant Temperature Molecular Dynamics Methods. *J. Chem. Phys.* **1984**, *81*, 511−519.
(108) Subedi, A.; Zhang, L.; Singh, D. J.; Du, M. H. Density Functional Study of FeS, FeSe, and FeTe: Electronic Structure, Magnetism, Phonons, and Superconductivity. *Phys. Rev. B: Condens. Matter Mater. Phys.* **2008**, *78*, 134514.

https://dx.doi.org/10.1021/acsnano.0c08429
ACS Nano 2021, 15, 6233−6242